Lithologically constrained velocity-density relationships and vertical stress gradients in the North Alpine Foreland Basin, SE Germany

Peter Obermeier[1], Florian Duschl[1], Michael C. Drews[1]

[1]Professorship of Geothermal Technologies, Technical University of Munich, Munich, 80333, Germany

Correspondence to: Michael C. Drews (michael.c.drews@tum.de)

Abstract. We systematically analysed density and velocity data from 4 boreholes to establish velocity-density relationships for the main lithological units in the North Alpine Foreland Basin in SE Germany. We applied these relationships to velocity data and spliced the resulting density values with actual density data and a shallow density model to retrieve complete density profiles along 55 deep wellbores, which at least penetrated the Cenozoic section in the study area. We integrated density profiles to vertical stress to investigate the spatial distribution of vertical stress gradients. Thereby, we observed an eastward decrease of vertical stress gradients, which correlates well with the geological configuration of the North Alpine Foreland Basin in SE Germany. Thereby, vertical stress gradient profiles can be reasonably estimated as a function of true vertical depth below ground level *TVD* in the western, central, and eastern parts of the study area using a power law relationship:

$$\text{West: } 21 \ \tfrac{MPa}{km} + \left(\tfrac{TVD}{325}\right)^{\frac{1}{1.80}}, \text{R}^2 = 0.98$$

$$\text{Central: } 21 \ \tfrac{MPa}{km} + \left(\tfrac{TVD}{410}\right)^{\frac{1}{1.93}}, \text{R}^2 = 0.99$$

$$\text{East: } 21 \ \tfrac{MPa}{km} + \left(\tfrac{TVD}{531}\right)^{\frac{1}{1.95}}, \text{R}^2 = 1.00$$

In addition, we also investigated the distribution of vertical stress gradients at the top of Upper Jurassic carbonates, an important aquifer for deep geothermal energy production. Our study, therefore, provides a valuable resource for future geophysical, geomechanical, and geological studies in the North Alpine Foreland Basin, both in a fundamental and applied research context.

1 Introduction

Knowledge of the stress field in the Earth's crust is a key prerequisite to understand geological processes and to mitigate risks associated with the economic usage of the subsurface (Allen and Allen, 2013; Zoback, 2007). Hereby, vertical stress is often assumed to be one of the principal stresses of the stress tensor and the first stress to

30 be estimated since its magnitude at any depth largely depends on the weight of the overlying material (Zoback, 2007). The weight of the overlying sediments can be estimated if the density of the material is known. Density in the subsurface can be determined along boreholes by measuring the energy loss between a gamma ray source and a detector (Asquith and Krygowski, 2004). The density of rocks thereby averages the density of the grains or matrix of the rock and the fluid stored in its pore space and is, therefore, directly related to the rock's porosity

35 (Asquith and Krygowski, 2004). Acoustic wave velocity through rocks or its inverse, the acoustic slowness, correlates well with density and porosity of different rock types. Several authors have investigated this correlation and established relationships that are widely used in geophysics and rock physics applications (e.g. Gardner et al., 1974; Raiga-Clemenceau et al., 1986; Wyllie et al., 1956). In sedimentary basins, the density typically increases with depth due to compaction (Allen and Allen, 2013), which also impacts the increased rate of vertical stress with

40 vertical depth below ground level, also known as vertical stress gradient. The intensification of compaction typically is highest at shallow depth before it converges towards grain or matrix densities of the buried sediments at greater depths. This reduction of porosity or increase of density with increasing depth has been previously described by exponential or logarithmic functions for sedimentary rocks (e.g. Athy, 1930; Sclater and Christie, 1980; Yang and Aplin, 2004; Couzens-Schultz and Azbel, 2014).

45 In this study, we investigate velocity-density relationships of main lithological units and the distribution of vertical stress gradients in the SE German part of the North Alpine Foreland Basin. To do this, we first correlate - depending on the lithological composition - acoustic velocities from high-resolution sonic logs with quality-controlled density logs from 41 wells by modifying Gardner's relationship (Gardner et al., 1974). We use these lithologically constrained velocity-density relationships to create density profiles in 55 boreholes with velocity data and

50 lithological information that have at least penetrated the entire Cenozoic basin fill. We complement these profiles with a shallow density model calibrated to density and density-transformed velocity data using an exponential density-depth relationship (Couzens-Schultz and Azbel, 2014). In a third step, these density profiles are integrated into vertical stress to acquire vertical stress gradient profiles at each of the 55 drilling locations. In addition, we derive geographically constrained vertical stress gradient models as a function of true vertical depth below ground

55 level using a power law relationship to provide a practical tool for future vertical stress modelling. The resulting distribution of vertical stress gradients is shown on maps and placed into context with the geological conditions and deep geothermal energy use in the North Alpine Foreland Basin in SE Germany.

2 The North Alpine Foreland Basin in SE Germany

The North Alpine Foreland Basin (NAFB) is located in Central Europe and extends from Lake Geneva in the West

60 to Upper Austria in the East (Kuhlemann and Kempf, 2002). Our study area encompasses the SE German (Bavarian) part of the NAFB. Here, the NAFB deepens towards the North Alpine Thrust Front (Fig. 1a), which separates the undeformed foreland part (Foreland Molasse) from the deformed part (Folded Molasse) and the Northern Alps (Fig. 1b). In front of the North Alpine Thrust Front, the Cenozoic basin fill of the NAFB reaches thicknesses of up to 5 km (Bachmann and Müller, 1992; Bachmann et al., 1987; Lemcke, 1973; Pfiffner, 1986).

65 This asymmetric wedge shape (Fig. 1b) was generated by the flexural subsidence of the European plate in consequence of the continental convergence of the African and European plates and is filled with Cenozoic molasse sediments (Bachmann and Müller, 1996; Bachmann et al., 1987; Pfiffner, 1986) (Fig. 2). The lateral extent of the Folded Molasse, which is largest in the western part of the study area, reflects the clockwise rotation of the North Alpine Thrust Front during late Oligocene – early Miocene and an associated westward increase of strain

70 (Ortner et al., 2015). Below the basin fill, Mesozoic passive margin sediments and Variscan crystalline basement rocks can be found (Bachmann et al., 1987).

While Upper Jurassic deposits are present in the entire study area, Lower Cretaceous, Upper Cretaceous and Eocene sediments are missing in the Western part, with a SE-NW increasing erosion (Bachmann et al., 1987). The sedimentary succession of the Cenozoic can be attributed to two transgressive-regressive megacycles, both of

75 which are defined by an eastward marine regression changing the depositional environment from a marine to a terrestrial setting (Fig. 2). Consequently, terrestrial sediments (sandstones) are dominating in the western part while marine sediments (shales and marls) prevail in the eastern part of the NAFB in SE Germany (Bachmann and Müller, 1996; Bachmann and Müller, 1992; Bachmann et al., 1987; Kuhlemann and Kempf, 2002). Since Late/Middle Miocene, sand and coarse-grained clastics were deposited (Kuhlemann and Kempf, 2002) (Fig. 2).

80 The NAFB in SE Germany has been extensively explored by the oil and gas industry in 1950-1980s (Bachmann et al., 1981; Lemcke, 1979) and more recently for deep geothermal energy extraction (Flechtner and Aubele, 2019; Schulz et al., 2017). Hereby, knowledge of stress magnitudes is critical to mitigate drilling and production risks such as wellbore instabilities and induced seismicity, in particular for deep geothermal energy drilling and production (Drews et al., 2022; Megies and Wassermann, 2014). Overall, more than 900 deep wells have been

85 drilled in the SE German part of the NAFB and along many of them density, sonic and/or seismic interval velocities were measured, but only became publicly accessible recently (Großmann et al., 2024). As a consequence, stress magnitudes and even the stress regime of the NAFB are subject to controversy in the scientific community. While this controversy mostly addresses the magnitudes of horizontal stresses (Budach et al., 2018; Drews and Duschl, 2022; Drews et al., 2019; Seithel et al., 2015; Von Hartmann et al., 2016; Ziegler and Heidbach, 2020), the actually

90 much easier vertical stress estimation has only been addressed and investigated by a few studies so far. Thereby, most studies estimated vertical stress as a necessary requirement to investigate other geomechanical phenomena. While some studies assumed a constant vertical stress gradient (Seithel et al., 2015) or average density values per stratigraphy (Budach et al., 2018) published from other areas of the NAFB (Leu et al., 2006), others introduced compaction dependent vertical stress estimates (Drews et al., 2018; Drews and Duschl, 2022; Drews et al., 2020;

95 Drews et al., 2019). Regional studies utilize numerical modelling to estimate vertical stress (Ahlers et al., 2021; Ahlers et al., 2022; Ziegler and Heidbach, 2020; Ziegler et al., 2016), but are subject to large uncertainties due to data limitations.
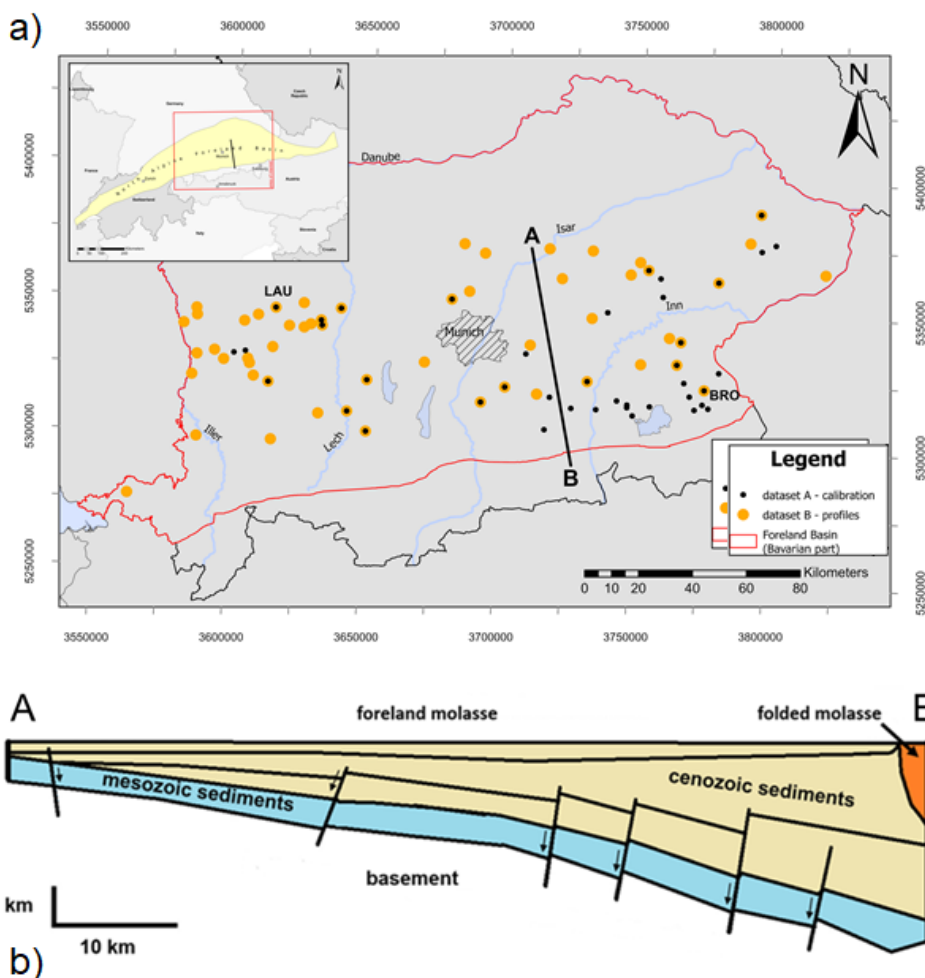
Figure 1: Location and overview of the study area and used well datasets. a) Study area (red outline) and used well
100 **locations for the calibration of the velocity-density transform (Dataset A with black markers) and for the generation of**
vertical stress gradient profiles (Dataset B with orange markers). The Lauterbach 1 (LAU) and Bromberg 1 (BRO)
wells are highlighted to showcase density profiles in Fig. 5b and c. The inset in the upper left corner shows an overview
map of the North Alpine Foreland Basin after Kuhlemann and Kempf (2002) and the area of interest (red box). b)
Cross-section (black line in Fig. 1a) showing the asymmetric basin geometry from north to south (after Reinecker et al.,
105 **2010).**

Only very few studies incorporated density and velocity data to analyse compaction or stress in the NAFB (Drews
et al., 2018; Drews and Duschl, 2022; Drews et al., 2020; Drews et al., 2019; Lohr, 1969, 1978). Lohr, 1969) and
Lohr (1978) found that seismic velocities in the NAFB increase towards the South and West and attributed this
effect to a general increase of stress magnitudes. Drews et al. (2018) and Drews et al. (2019) fitted an Athy-type
110 porosity decay function (Athy, 1930) modified for vertical effective stress to an average density profile based on
density and velocity data from a few wells to integrate vertical stress profiles. They also found that Gardner's
average velocity-density relationship (Gardner et al., 1974) reasonably captures the velocity-density correlation of
sediments in the NAFB in SE Germany, but only presented a model, which reflects the average density profile
along the investigated wells. Drews and Duschl (2022) used the same Athy-type porosity decay function to model

115 vertical stress in 18 deep wells distributed along both sides of the North Alpine Thrust Front. They found that
vertical stress gradients are mainly increasing towards the North Alpine Thrust Front and southward of it, and, in
a less pronounced fashion, also from East to West. Drews and Duschl (2022) interpreted the southward increase
as a result of increased horizontal compaction towards the Alps and the eastward decrease to reflect changes in
lithological composition and undercompaction due to overpressure presence.

120
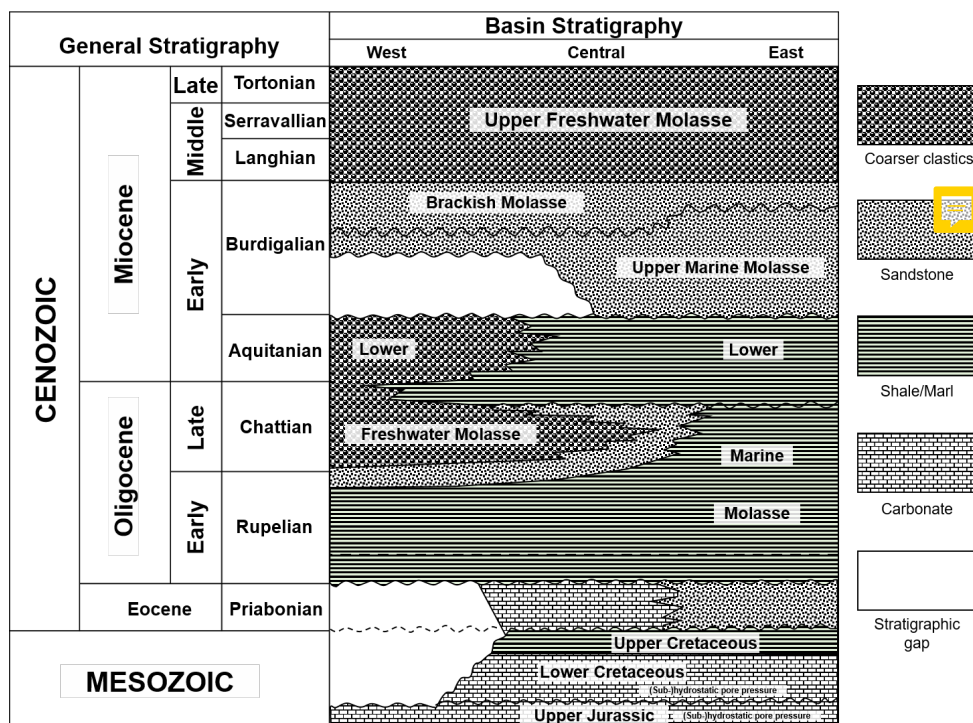
**Figure 2: Chronostratigraphic chart of the North Alpine Foreland Basin in SE Germany modified from Drews et al.
(2018) after Kuhlemann and Kempf (2002) and Bachmann and Müller (1992).**

Overpressure in the NAFB is present due to high sedimentation rates during Late Oligocene and Early Miocene
125 times (Drews et al., 2018; Zweigel, 1998) and can be found in Oligocene and Upper Cretaceous sediments (Drews
et al., 2018; Müller and Nieberding, 1996; Müller et al., 1988), which is reflected by low interval velocities and
electrical resistivities (Drews et al., 2018; Drews and Duschl, 2022; Rizzi, 1973; Shatyrbayeva et al., 2024). Since
disequilibrium compaction is believed to be the main overpressure mechanism (Drews et al., 2018; Drews et al.,
2020), the presence of overpressure possibly impacts density and, thus, vertical stress. Overpressure appears in the
130 south and south-eastern parts of the study area and roughly follows the distribution of Upper Cretaceous shales,
which are missing in the north-western part of the study area (Drews et al., 2018; Shatyrbayeva et al., 2023;
Shatyrbayeva et al., 2024). The top of overpressure is usually tied to the top of Oligocene shales and is not found
at depths above 1500 m below ground level (Drews et al., 2018; Shatyrbayeva et al., 2023). In contrast, Lower
Cretaceous and Upper Jurassic carbonates roughly follow the hydraulic head of the Danube River in the North
135 over geological timescales and are underpressured (Lemcke, 1976), which results in a sharp pressure regression if
the overburden is overpressured (cf. Drews et al., 2022).

3 Data and methods

In total, the dataset comprises of 78 deep oil and gas wells drilled in the North Alpine Foreland in SE Germany (cf. Großmann et al., 2024 for a detailed description of the data sources). We split the dataset into two subsets to

140   a) establish lithologically constrained velocity-density relationships (Dataset A) and to b) use these relationships to generate and model continuous density and vertical stress profiles along deep wells in the NAFB in SE Germany (Dataset B) (Fig. 1a and Table 1). Dataset A contains 41 wells with overlapping sonic velocity and density data from geophysical borehole measurements and lithological information from cutting descript[OFS] Dataset B encompasses 55 wells which have at least penetrated the entire Cenozoic basin fill and which have either measured

145   density, sonic velocity or seismic interval velocity in addition to lithological information from cutting descriptions. Seismic interval velocities are derived from vertical seismic profiles and checkshots. Information on stratigraphic tops and cutting descriptions are extracted from geological end of well reports. In addition, wells of Dataset B are not allowed to have data gaps larger than 30 m except for the shallow section (< 1500 m vertical depth below ground level). Eighteen wells are part of both Dataset A and Dataset B (Table 1).

150

Table 1: Wellnames, well locations, dataset membership and coverage of considered data sources for complete density profiles in percent.

Wellname	Easting [GK-Zone3]	Northing [GK-Zone3]	Dataset	ρ_b [%]	DT [%]	V_{int} [%]	Shallow ρ_b-model [%]
Aitingen 1	3633108	5343026	A + B	72	17	7	4
Allershausen 1	3693032	5370061	B	0	0	72	28
Almertsham C3	3747589	5315874	A	-	-	-	-
Altensteig 1	3614191	5319589	A + B	19	67	11	3
Anzing 3	3710871	5336680	B	0	92	7	1
Arlesried 1	3601094	5329898	A	-	-	-	-
Attel 1	3732498	5323993	A + B	17	66	14	3
Balzhausen 1	3609710	5344235	B	0	48	45	7
Birnbach 5	3800774	5376767	A	-	-	-	-
Bodenkirchen 1	3753875	5365979	A + B	39	39	20	2
Bonbruck 1	3750695	5368819	B	0	0	87	13
Brombach 1	3795599	5374319	A	-	-	-	-
Bromberg 1	3776038	5322287	A + B	21	67	10	2
Buch 1	3587080	5343460	B	0	0	84	16
Dietershofen 1	3586760	5346050	B	0	0	84	16
Doepshofen 1	3626512	5349133	B	0	0	76	24
Eggstaett C1	3755955	5315546	A	-	-	-	-
Eigelwald 1	3762453	5341158	B	0	89	6	5
Elbsee 1	3615871	5298328	B	0	0	95	5
Emmersdorf 1	3794880	5388036	A + B	73	23	3	1
Endlhausen 1	3693234	5314903	A + B	50	45	5	0
Erisried 1	3608609	5321614	B	0	76	18	6
Frickenhausen 1	3597410	5327330	B	0	59	31	10
Fuessing 1	3819610	5366465	B	0	0	88	12
Garching 1	3766720	5339770	A + B	28	63	7	2
Giftthal 1	3747313	5364083	B	0	78	13	9
Grucking 1	3721857	5361744	B	0	0	66	34
Haimhausen 2	3687679	5355705	B	0	36	42	22
Hebertshausen 1	3681210	5352544	A + B	44	49	4	3
Heimertingen 1	3585770	5321430	B	0	0	99	1
Hofolding 1	3702024	5320847	A + B	17	76	7	0
Irlach C1	3743720	5317263	A	-	-	-	-
Isen-Dogger 1	3733480	5347448	B	0	91	7	2
Jedesheim 1	3582140	5340380	B	0	0	63	37
Kaufbeuren 1	3633043	5308573	B	0	0	49	51
Kinsau 2	3643758	5309716	A + B	3	90	5	2
Kirchheim C1	3781222	5328779	A	-	-	-	-
Kirchisen 1	3759503	5356241	A	-	-	-	-

Klosterbeuren 1	3593930	5330640	B	0	0	82	18
Lauterbach 1	3616090	5347049	A + B	34	29	21	16
Legau 1	3588180	5298680	B	0	0	100	0
Mattenhofen 1	3713917	5318622	B	0	83	16	1
Mering 1	3640312	5347661	A + B	90	10	0	0
Mittelstetten 1	3633449	5341164	A + B	66	7	24	3
Moosburg 1	3716841	5372652	B	0	0	83	17
Muenchsdorf 1	3732941	5372432	B	0	0	55	45
Oberrieden 1	3606340	5327840	B	0	0	94	6
Opfenbach 1	3563310	5276740	B	0	86	13	1
Pfarrkirchen 1	3791305	5377281	B	0	85	6	9
Pierling A1	3770615	5319752	A	-	-	-	-
Pless 2	3587430	5329040	B	0	87	9	4
Poering 1	3709405	5333378	A	-	-	-	-
Reichertshausen 1	3685237	5373265	B	0	39	14	47
Rettenbach C1	3772592	5314865	A	-	-	-	-
Rieden 3	3605344	5330686	A	-	-	-	-
Rimsting C1	3749730	5311951	A	-	-	-	-
Scherstetten 1	3621332	5340584	B	0	0	86	14
Schmidhausen A2	3726856	5313867	A	-	-	-	-
Schnaitsee 7	3752143	5331016	B	0	67	21	12
Schongau 1	3651010	5302504	A + B	25	66	6	3
Schwabegg 1	3626859	5340150	B	0	0	89	11
Schwabmuenchen 1	3629287	5341453	B	0	0	96	4
Seeham C1	3717215	5305624	A	-	-	-	-
Soehl 1	3718770	5317643	A	-	-	-	-
StLeonhard C1	3777709	5315529	A	-	-	-	-
Tacherting 1	3765537	5331338	A + B	9	84	6	1
Teisenham 1	3747561	5314926	A	-	-	-	-
Teising 1	3758436	5363071	A	-	-	-	-
Trostberg A1	3768410	5324674	A	-	-	-	-
Unterbrunn 1	3671892	5328896	B	0	0	96	4
Unterkammlach 1	3607030	5326190	B	0	0	88	12
Utting 2	3650760	5321594	A + B	0	94	5	1
Walchenberg 1	3775455	5316870	A	-	-	-	-
Weitermuehle1 1	3739183	5349822	A	-	-	-	-
Winzer 1	3604690	5341805	B	0	22	70	8
Wurmannsquick 1	3779989	5362316	A + B	13	77	0	10
Zaisertshofen 1	3615464	5332448	B	0	0	87	13
Zaissberg C4	3736126	5313742	A	-	-	-	-

ρ_b: quality-controlled density data from density log; DT: sonic velocity data from sonic log; V_{int}: seismic interval velocity data from vertical seismic profiles of checkshots; Shallow ρ_b-model: shallow density model (equation 4)

In order to establish lithologically constrained velocity-density relationships and to generate and model vertical stress gradient profiles, we follow a four-step workflow, which will be explained in more detail in the subsections below:

1. Retrieving standardized **lithological information** and **quality control of density data**

2. Establishing lithologically constrained **velocity-density relationships** based on wellbores, along which both density and sonic velocity have been measured

3. Generation of complete **density profiles** along wellbores which at least penetrated the Cenozoic basin fill by splicing density data and density-transformed velocity data (using the velocity-density relationships from step 2) with modelled densities in the shallow section; this step includes a homogenisation of litho-stratigraphic information from cutting descriptions with density and sonic/seismic velocity data from geophysical borehole logging

4. Integration of continuous density profiles from step 3 to calculate **vertical stress gradient profiles** and establishing practical **vertical stress gradient models** as a function of true vertical depth below ground level

3.1 Lithological information and quality control of density data

3.1.1 Lithological information

170 Lithological information is required to constrain lithology-dependent velocity-density relationships and to use these relationships to transform velocity to density where no measured density data was available. We grouped lithological information from cutting descriptions of Mesozoic and Cenozoic sections of the analysed wells into five main lithological units: coarse-grained clastics (gravel and conglomerates), carbonates (limestones, dolostones), sandstones (clean, marly or clayey calcareous and siliciclastic sandstones and siltstones), marls (clean, silty or sandy marls) and shales (clean, silty or marly clays and claystones). Other lithologies, such as coal, have only been recorded in accessory amounts and are neglected in our study.

Two deep wells in the southwest of the study area, Heimertingen 1 and Legau 1, only have little or no lithological information from cutting descriptions or core samples. However, both wells are important for geographic coverage of the study area, and we generated average synthetic lithological columns based on the information of the immediate offset wells.

3.1.2 Quality control of density data

Density data in the NAFB is often impeded by borehole breakouts and washouts (cf. Reinecker et al., 2010). Since the density tool requires physical contact with the borehole wall, the quality of density data is challenged in these intervals. To exclude sections of questionable quality from the density dataset, we use two quality measures:

185   1.   The ratio between the actual borehole diameter from the caliper log and the used drill bit size is not allowed to exceed a critical value of 1.10

     2.   The bulk density correction value *DRHO*, which is an indicator of the quality of the measurement at each data point, has to be lower than 0.05

These strict cut-off values delimit the amount of utilized density-sonic data pairs by 51 % but simultaneously ensure reproducible data quality.

3.2 Lithologically constrained velocity-density relationships

We establish lithologically differentiated velocity-density relationships by fitting Gardner's relationship (Gardner et al., 1974) to Dataset A:

195
$$\rho_b = A * \left(V_p * 3.281\right)^B \tag{1}$$

Where ρ_b is the modelled density value in *g/cm³*, V_p is the sonic or seismic interval velocity in *m/s* and *A* and *B* are lithology-dependent constants, which, according to Gardner et al. (1974), provide a reasonable fit to mixed lithology datasets, if *A* and *B* are set to 0.23 and 0.25, respectively. We fit equation 1 to our lithologically
200 differentiated Dataset A by changing *A* and *B* such that the sum of the squared differences between the calculated and measured densities becomes minimal. For realistic ranges of density (1.5-3.0 g/cm³) and interval velocity (1500-6000 m/s), *A* and *B* will result in value combinations which follow a logarithmic relationship (Fig. 3):

$$B = a * \ln(A) + b \tag{2}$$

205

Where *a* and *b* define the curvature of the relationship and the minimum value of *B* and typically takes values of ~-0.11 and ~0.08 for the mentioned parameter space, respectively (Fig. 4). Thereby, low *A* and high *B* combinations refer to steep velocity-density relationships which are typical for softer, "compressible materials". In contrast, high *A* and low *B* combinations reflect sediments where density is not changing as fast with velocity, which is typical for more competent or "incompressible materials" (cf. Gardner et al., 1974).
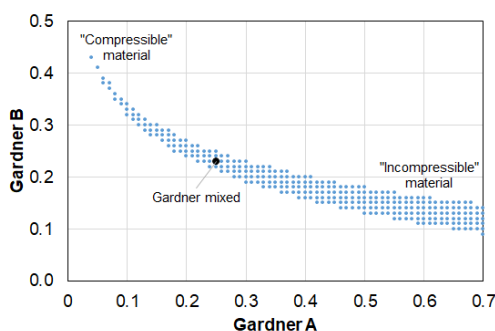
Figure 3: Mathematically possible range for Gardner A and B (blue markers) for realistic densities (1.5-3.0 g/cm³) and velocities (1500-6000 m/s) with a step size of 100 m/s. The black dot marks the A-B combination for mixed lithologies after Gardner et al. (1974).

3.3 Continuous density profiles

Along each well of Dataset B, we generate continuous density profiles, which cover the entire Cenozoic basin fill and, if present, sediments of Cretaceous age. We generate a homogenised dataset with quality-controlled density data, sonic and seismic interval velocity data and litho-stratigraphic information from cutting descriptions from Dataset B. Since the cutting descriptions apply to larger intervals than the measured density and velocity data, we defined a desired interval length of 2 m. Each interval must cover only a single stratigraphic and lithological section, which might result in slight deviations from the desired 2-m-interval size.

The generation of continuous density profiles follows a hierarchical approach. Quality-controlled density logs are the preferred data source. Gaps in the quality-controlled density logs are then primarily filled by transforming first sonic velocity and second seismic interval velocity to density using Gardner's relationship (Gardner et al., 1974; equation 1) with lithologically constrained *A* and *B* parameters according to the main lithological unit of the depth interval. The remaining gaps with intervals > 30 m, which are exclusively present in the shallow section (*TVD* < 1500 m), are filled with a lithology-dependent density model, which we fit to available shallow density data from all wells. Finally, we apply a 30 m moving average window filter to the entire spliced density dataset to smooth outliers and to close remaining data gaps.

3.3.1 Density from checkshots and vertical seismic profiles

In intervals where neither density nor sonic velocity data are available, seismic interval velocity from checkshots or vertical seismic profiles is converted to density. However, intervals measured by vertical seismic profiles or checkshots often cover several depth intervals with different main lithological units. Here, we estimate Gardner's *A* by calculating an average weighted by the thickness h_{MLU} of each main lithological unit *MLU* covered by the measured velocity interval $dTVD_{V_p}$:

$$A\left(dTVD_{V_p}\right) = \frac{1}{dTVD_{V_p}} \sum_{i=1}^{i=5} h_{MLU_i} * A_{MLU_i} \tag{3}$$

240   Where A_{MLU_i} is Gardner's A of the ith main lithological unit MLU and the sum of all thicknesses of all main lithological units is $dTVD_{V_p}$. Subsequently, Gardner's B is derived by using A_{MLU_i} in equation 2.

3.3.2 Shallow density profiles

Intervals without any measured log data over a length of more than 30 m only occur in shallow well sections. Since these intervals are above the shallowest recorded top of overpressure of 1500 m (cf. Drews et al., 2018;

245   Shatyrbayeva et al., 2023), we model density ρ_b in these intervals as a function of true vertical depth below ground level TVD in m for each defined main lithological unit (Couzens-Schultz and Azbel, 2014):

$$\rho_b = \rho_{max} - \left(\rho_{max} - \rho_{surf}\right) * exp\left(-\frac{TVD}{C}\right) \tag{4}$$

250   Where ρ_{max} is the maximum density occurring above a TVD <1500 m, ρ_{surf} the average surface density and C a compaction constant. We then fit equation 4 for each main lithological unit to density-depth pairs from all wells with respective data above 1500 m and an interval size of 1 m by adjusting ρ_{max}, ρ_{surf} and C and by minimizing the sum of squared differences between the measured and modelled densities.

3.4 Vertical stress gradient profiles and models

255   **3.4.1 Integration of density to vertical stress and calculation of vertical stress gradient profiles**

Vertical stress S_v in MPa at any true vertical depth below ground level TVD in km is calculated by integrating the weight of the overlying material:

$$S_v(TVD) = \int_0^{TVD} \rho_b(TVD) * g * dTVD \tag{5}$$

260

Where g is the Earth's gravitational acceleration at 9.81 m/s². We then calculate vertical stress gradients by dividing S_v by TVD in km:

$$\nabla S_v = \frac{S_v}{TVD} \tag{6}$$

265

Where ∇S_v is the vertical stress gradient in MPa/km.

3.4.2 Vertical stress gradient modelling

We model the vertical stress gradient as a function of TVD using a power law relationship:

270      $$\nabla S_v^* = \nabla S_v^0 + \left(\frac{TVD}{\alpha}\right)^{\frac{1}{\beta}} \tag{7}$$

Where ∇S_v^* is the modelled vertical stress gradient at TVD and ∇S_v^0 is the starting vertical stress gradient close to surface. α and β are fitting parameters which we determine by minimizing the sum of the squared differences between actual and modelled vertical stress gradients.

4 Results and discussion

4.1 Velocity-density relationships for the main lithology units in the NAFB

The calibration of Gardner's A and B (Gardner et al., 1974) to data pairs of quality-controlled density and sonic velocity measurements of Dataset A results in distinct A-B combinations for the investigated main lithological units, which fall into the corridor of realistic velocity-density combinations (Fig. 4a). The correlation between A and B can be described by a logarithmic relationship (cf. Fig. 4 and equation 2), where for our Dataset A, a and b of equation 2 become -0.105 and 0.0966, respectively (Fig. 4a). Hereby, the established trendline plots at the upper limit of possible A-B combinations and slightly above Gardner's mixed lithology combination of $A = 0.25$ and $B = 0.23$ (Fig. 4a), showing that density of the investigated main lithological units in the study area increases rather fast with velocity. This observation might indicate that the investigated main lithological units are either generally more compressible or that their compaction is additionally affected by mechanisms other than burial and vertical loading. Compaction mechanisms other than burial have also been hypothesized by previous authors who investigated the distribution of overpressure and stress in the NAFB (Drews and Duschl, 2022; Drews et al., 2020; Lohr, 1969, 1978; Müller and Nieberding, 1996; Shatyrbayeva et al., 2024).

In addition to the relationship between Gardner's A and B parameters, our results also confirm that stiffer or rather incompressible lithologies such as coarse-grained clastics (Fig. 5b) and carbonates (Fig. 5c) follow a less steep (higher A, lower B) velocity-density relationship when compared to marls (Fig. 5d), sandstones (Fig. 5e) and shales (Fig. 5f), whose velocity-density relationships can be described with lower A and higher B values. The results also indicate that marls and sandstones show very similar properties and velocity-density relationships.

It should be noted that the resolution of lithological information from cutting descriptions is typically ≥ 5m, which might result in the mixing of lithologies where the lithological variations are below this resolution. Thin-bedded intercalations of sandstones and marls have been especially reported for late Oligocene and early Miocene sediments in the western and central part of the study area (Kuhlemann and Kempf, 2002) and might explain the similarity in our results between marls and sandstones. Also, it is important to understand that we assume that that the grouped and investigated main lithological units are representative for the entire study area. However, the basin fill of the NAFB is a result of different routing systems with variable mineralogical composition of the respective sources (Kuhlemann and Kempf, 2002), which might explain the rather large uncertainty around the fitted velocity-density relationships. Nevertheless, since we grouped several lithologies, we believe that our results represent valid average relationships on a basin-scale. Also, due to lack of high-quality density data it was not possible to investigate sub-regional variations.
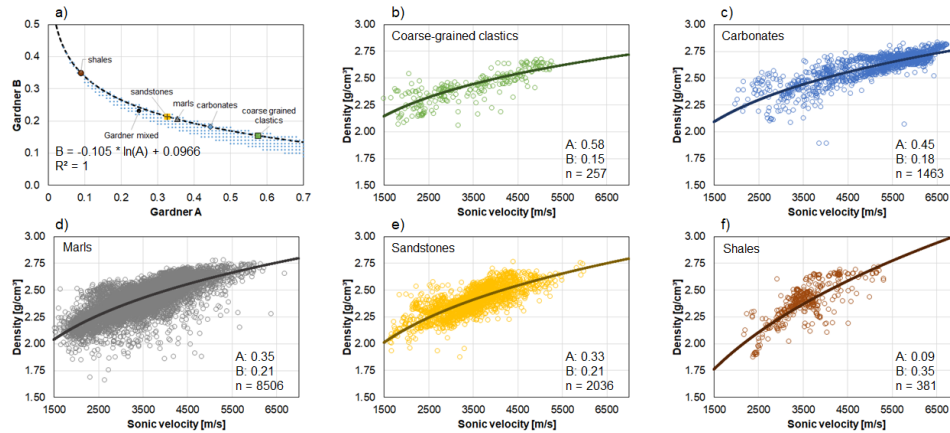
Figure 4: Lithologically calibrated velocity-density relations based on Gardner et al. (1974). a) Relationship between A-B-parameters for the main lithological units. A-B-parameters were fitted to quality-controlled velocity-density-relations for b) coarse-grained clastics, c) carbonates, d) marls, e) sandstones and f) shales.

4.2 Density profiles

Based on the established values for Gardner's A and B parameters for the main lithological units of the SE German part of the NAFB (cf. Fig. 4), sonic and seismic interval velocities have been transformed to density and spliced with quality-controlled density data for each well of Dataset B. Remaining gaps with intervals ≥ 30 m are exclusively left in the shallow section ($TVD \leq 1500$ m). To fill these gaps, we fitted equation 2 to shallow density and transformed density (from sonic or seismic interval velocity) data from all wells for each main lithological unit (Fig. 5a). The fitting values for the varied parameters ρ_{max}, ρ_{surf} and C are listed in Table 2. In concordance with the established velocity-density relationships (cf. Fig. 4) shales show the fastest compaction (highest compressibility) and lowest surface density (Fig. 5a). Compaction in the shallow section is very similar for all other main lithological units except for carbonates, which compact fast towards high densities close to grain densities of carbonates (cf. Gardner et al., 1974).

Table 2: Shallow (<1500 m) density modelling parameters for the main lithological units.

Shallow density modelling parameter	Coarse-grained clastics	Carbonates	Sandstones	Marls	Shales
Maximum density ρ_{max} [g/cm³]	2.39	2.93	2.43	2.45	2.29
Surface density ρ_{surf} [g/cm³]	2.22	2.16	2.07	2.14	1.80
Compaction coefficient C	246.59	1542.50	405.40	504.76	272.10

Complete density profiles after splicing quality-controlled density data, densities transformed from sonic and seismic interval velocities and the shallow density model show reasonable alignment between the different data sources (Fig. 5a and b). The largest deviations are observed towards higher densities from transformed vertical seismic profiles and checkshots (cf. elevated densities from seismic interval velocities at 400 m and 500 m in Fig. 5a and b, respectively), which could be due to mixing of several main lithological units within the measured intervals or the typically lower acoustic wave frequency of these measurements, when compared to sonic velocity measurements (cf. Zoback, 2007). Although we applied rather rigorous cutoffs for borehole enlargements and density corrections to quality-controlled density data, obvious outliers remain (cf. negative spikes of density data at 1070 m in Fig. 5b and between 1400 m and 1750 m and at 4100 m in Fig. 5c). However, for subsequent vertical

stress integration a moving average window of 30m was applied to remove these outliers and to close remaining gaps with intervals ≤ 30 m (black lines in Fig. 5a and b), resulting in realistic and complete average density profiles.

335
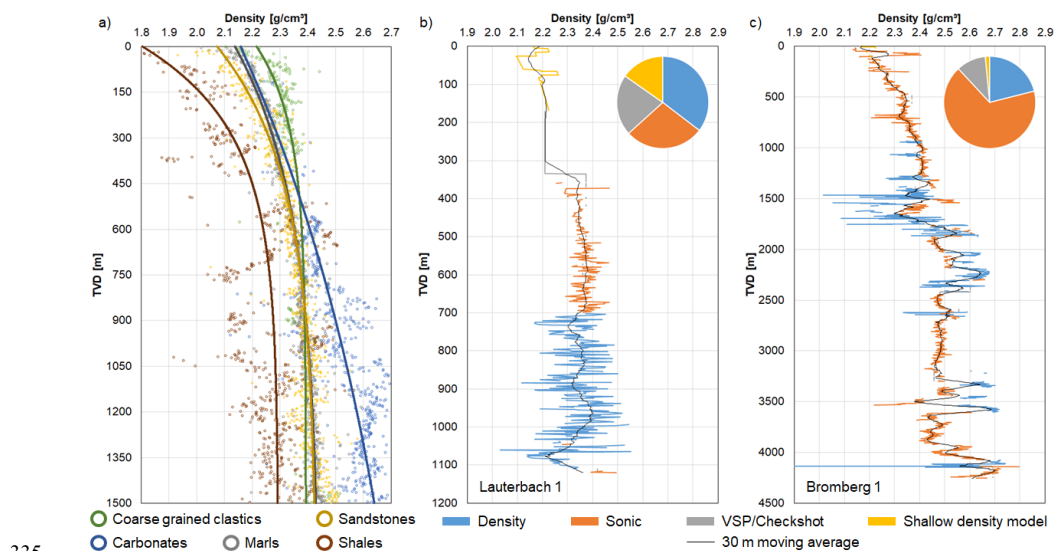
Figure 5: Density profiles. a) Shallow density profiles for each main lithological unit (lines) fitted to quality-controlled and transformed density data from all wells with available data. b) Example of a spliced and averaged density profile for the shallow Lauterbach 1 well in the north-western part of the study area (LAU in Fig. 1a). c) Example of a spliced and averaged density profile for the deep Bromberg 1 well in the south-eastern part of the study area (BRO in Fig. 1a).
340 **The pie chart insets of b) and c) indicate the coverage by quality-controlled density data (blue), density-transformed sonic velocity (orange) and seismic interval velocity from vertical seismic profiles (VSP) or checkshots (gray) and the shallow density model (yellow).**

4.3 Vertical stress gradient distribution in the NAFB

Vertical stress gradients were calculated after integrating the complete density profiles at each well location of
345 Dataset B to vertical stress. Vertical stress gradients are decreasing from west to east, which is in concordance with previous investigations of vertical stress gradients along the North Alpine Thrust Front (Drews and Duschl, 2022). While this trend is less pronounced at shallower depths (Fig. 6a), wells in the western part of the study area display vertical stress gradients which are up to 1.5 MPa/km higher when compared to wells located in the east of the study area at greater depths (Fig. 6b and Fig. 6c). At 3 km true vertical depth below ground level, this gradient
350 difference can cumulate to absolute vertical stress magnitude differences of 4.5 MPa. Note that since the NAFB is deepening from north to south in the study area, less wells become available with each horizontal slice through the vertical stress gradient distribution.

While the increase of vertical stress gradients with depth simply reflects increasing compaction and with it the loss of porosity and an increase of density (cf. Allen and Allen, 2013), the reasons for the eastward decrease of vertical
355 stress gradients are more complex. First, the lithological composition of sediments of Lower Oligocene (Rupelian) to Lower Miocene (Aquitanian) age is significantly changing from west to east in the study area: coarser grained terrestrial material was deposited in two regressions in the western part, while a marine setting prevailed in the eastern part of the study area, resulting in the deposition of fine-grained sediments. The central part was subject to a transitional depositional environment during that time (Kuhlemann and Kempf, 2002). Shales, which are typical
360 deposits from a marine environment, display the lowest densities in our study area, which could be a significant factor for lower vertical stress gradients in the eastern part of the study area (cf. Fig. 4). The abundance of shales

in the eastern part of the study area compared to the western part is also pronounced by the presence of Upper Cretaceous shales, which are missing due to erosion in the western part (Bachmann et al., 1987). The presence of shales, also fostered the development of significant pore fluid overpressure in the eastern part of the study area (Drews et al., 2018). Here, the main postulated mechanism for overpressure formation is disequilibrium compaction, which results in abnormally high porosity and possibly low density in the overpressured zone. The overpressured section can be up to 2 km in thickness in the eastern part of the study area (Drews et al., 2018; Drews and Duschl, 2022) and disequilibrium compaction could therefore be a main factor for reduced vertical stress gradients in the area. In addition, the western part is also subject to higher horizontal strain rates, which is reflected by the decreased N-S extent of the NAFB and a more pronounced deformation front (Folded Molasse) along the North Alpine Thrust Front in this area (Ortner et al., 2015; Drews and Duschl, 2022). Elevated horizontal strain combined with lower pore pressures and higher permeability of the basin fill would also foster sediment compaction and therefore favor lower porosities, higher densities and finally higher vertical stress gradients.

We also show the distribution of vertical stress gradients at the top of the Upper Jurassic (Fig. 6d), which is an important thermal aquifer for deep geothermal energy utilization in the NAFB (Flechtner and Aubele, 2019; Schulz et al., 2017). In addition to the aforementioned eastward reduction, also an apparent southward increase in vertical stress gradients can be observed, reflecting the southward dip and associated increasing depth of the Upper Jurassic in the study area. Our results highlight the importance of careful vertical stress gradient estimation for geomechanical studies of the Upper Jurassic aquifer, e.g. to mitigate the risk of induced seismicity (Megies and Wassermann, 2014): depending on the location of a deep geothermal energy project, vertical stress gradients can differ by up to 3 MPa/km at the top of the Upper Jurassic. Utilization of a simplified and constant vertical stress gradient (e.g. 23 MPa/km) is therefore not recommended to accurately plan safe geothermal production.
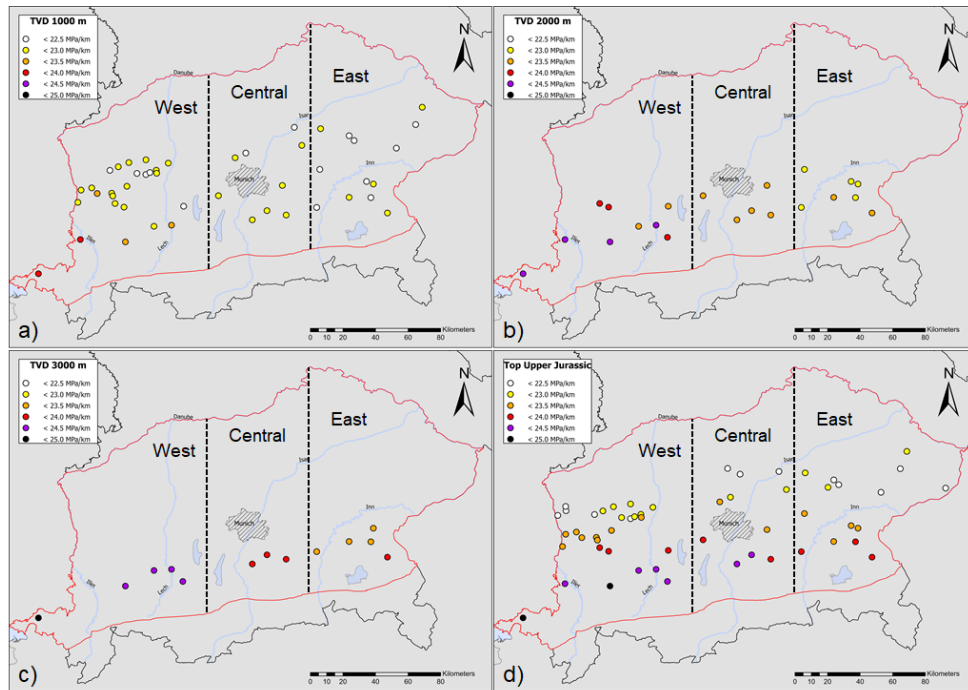
Figure 6: Distribution of vertical stress gradients in MPa/km in the North Alpine Foreland Basin. Vertical stress gradient distribution at a true vertical depth below ground level a) TVD = 1000 m, b) TVD = 2000 m, c) TVD = 3000 m d) Vertical stress gradient distribution at the top of Upper Jurassic carbonates. The N-S trending dashed black lines divide the study area in a western, central and eastern part.

4.4 Vertical stress gradient modelling

In order to provide practical vertical stress gradient models for the SE German part of the NAFB, we model vertical stress gradients as a function of *TVD* and geographical easting. Thereby, we divide the study area into a western, central and eastern subdivision (Fig. 6) to account for the lithological variations in the Cenozoic section and their impact on compaction (Bachmann and Müller, 1992; Bachmann et al., 1987; Kuhlemann and Kempf, 2002) (cf. Fig. 2). We calculate the arithmetic mean of vertical stress gradients of all wellbores of Dataset B within these three subdivisions using a 500 m step size with a tolerance of +/- 2 m. We restrict the calculation of the average to a maximum depth of *TVD* = 3500 m, because only very few wells drilled into greater depths, and to avoid bias towards single wells. Fig. 7a shows the three resulting vertical stress gradient models (cf. equation 7) fitted to the mean vertical stress gradients in the western, central and eastern parts. Both the mean vertical stress gradients and fitted models capture the eastward decrease of vertical stress gradients in the study area.

Due to its relevance for deep geothermal energy production in the NAFB, we also established vertical stress gradient models for the top of the Upper Jurassic (Fig. 7b) using equation 7. Likewise, both the vertical stress gradients established through density integration and modelling reflect the eastward decrease of vertical stress gradients and provide a simple tool to more accurately estimate vertical stress for future geomechanical studies, e.g. to mitigate the risk of induced seismicity due to fluid injection.
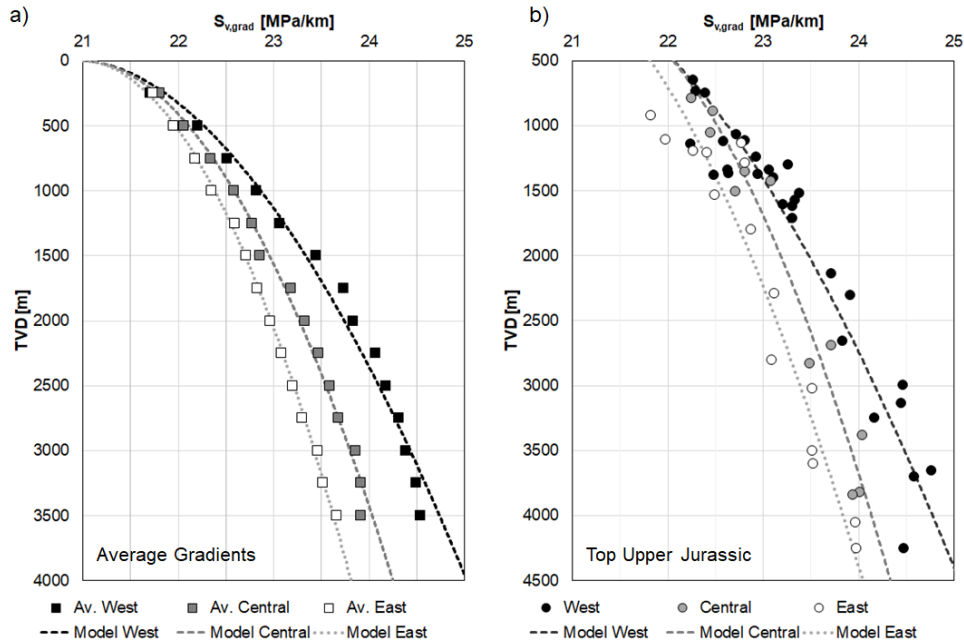
405

Figure 7: Vertical stress gradients from Dataset B as a function of true vertical depth below ground level *TVD*. a) Average and modelled vertical stress gradients in the western, central and eastern part of the study area (cf. Fig. 6). Average vertical stress gradients reflect the arithmetic mean from all wells in the western, central and eastern part of the study area at 14 depths and with a step size of 500 +/- 2 m. b) Well-based and modelled vertical stress gradients in the western, central and eastern part of the study area at the top of the Upper Jurassic.

410

The fitting parameters α and β along with the coefficient of determination for both the average vertical stress gradient models and the top Upper Jurassic vertical stress gradient models are listed in Table 3. For all models the starting vertical stress gradient close to the surface ∇S_v^0 was set to 21 MPa/km.

415   **Table 3: Parameters to model vertical stress gradients for Dataset B.**

Vertical stress gradient model	∇S_v^0 [MPa/km]	α	β	R²
Average (entire study area)		381	1.91	0.99
Average (West)		325	1.80	0.98
Average (Central)		410	1.93	0.99
Average (East)	21.0	531	1.95	1.00
Top Upper Jurassic (West)		451	1.64	0.91
Top Upper Jurassic (Central)		449	1.91	0.96
Top Upper Jurassic (East)		706	1.66	0.89

∇S_v^0, α and β: vertical stress gradient close to the surface and fitting parameters (equation 7);
R²: coefficient of determination

5 Conclusions

Based on Gardner's relationship, we established regional velocity-density relationships for the main lithological units of the North Alpine Foreland Basin in SE Germany. We used these relationships to generate complete density profiles along 55 wells, which at least penetrated the entire Cenozoic section to integrate vertical stress and to calculate vertical stress gradients. Thereby, the following observations were made:

- Density data is often impeded by washouts and/or breakouts and has to be rigorously quality-controlled
- Velocity-density relationships differ for the main lithological units, but can be approximated by modifying the A and B parameters of Gardner's relationship
- Calibrated A and B parameters of Gardner's relationship for each main lithological unit follow a logical sequence on a logarithmic relationship: more compressible rocks such as shales and marls display a steeper velocity-density relationship with lower A and higher B values, while the opposite is the case for less compressible rocks such as carbonates and coarse-grained clastics
- Vertical stress gradients decrease from west to east in the SE German part of the North Alpine Foreland Basin, correlating well with lithological variations, overpressure and tectonics

In addition, we provided applicable vertical stress gradient models for the western, central and eastern parts of the study area, which can be used to either calculate vertical stress profiles in these parts or vertical stress gradients at the top of Upper Jurassic carbonates, which pose an important aquifer for deep geothermal energy production. Our results, therefore, provide a useful resource for future geophysical, geomechanical and geological studies in the North Alpine Foreland Basin, which require velocity-density relationships and an estimate of vertical stress.

Data availability

The data used in this study is available upon request from the Bavarian Environment Agency.

Author contribution

PO: Conceptualization, investigation, formal analysis, writing of the original draft

FD: Supervision, conceptualization, writing – review & editing

MCD: Supervision, conceptualization, writing – review & editing, funding acquisition

Competing interests

The authors declare that they have no conflict of interest.

Acknowledgements

The presented study was funded by the Bavarian Environment Agency through the research project KompakT and the Bavarian Ministry for Science and the Arts through the framework of the Geothermal-Alliance Bavaria (GAB). The authors would like to thank Johannes Großmann (Bavarian Environment Agency) for the support in data acquisition.

References

Ahlers, S., Henk, A., Hergert, T., Reiter, K., Müller, B., Röckel, L., Heidbach, O., Morawietz, S., Scheck-Wenderoth, M., and Anikiev, D.: 3D crustal stress state of Germany according to a data-calibrated geomechanical model, Solid Earth, 12, 1777-1799, 10.5194/se-12-1777-2021, 2021.

Ahlers, S., Röckel, L., Hergert, T., Reiter, K., Heidbach, O., Henk, A., Müller, B., Morawietz, S., Scheck-Wenderoth, M., and Anikiev, D.: The crustal stress field of Germany: a refined prediction, Geothermal Energy, 10, 10.1186/s40517-022-00222-6, 2022.

Allen, P. A. and Allen, J. R.: Basin Analysis: Principles and Application to Petroleum Play Assessment, 3rd Edition, Wiley-Blackwell, 632 pp.2013.

Asquith, G. and Krygowski, D.: Basic well log analysis, Second Edition, AAPG Methods in Exploration, The American Association of Petroleum Geologists, Tulsa, Oklahoma2004.

Athy, L. F.: Density, porosity and compaction of sedimentary rocks, AAPG Bulletin, 14, 1-24, 1930.

Bachmann, G. H. and Müller, M.: Sedimentary and structural evolution of the German Molasse Basin, Eclogae Geologicae Helvetiae, 85, 519-530, 1992.

Bachmann, G. H. and Müller, M.: Die Entwicklung des süddeutschen Molassebeckens seit dem Variszikum: Eine Einführung, Zeitschrift für Geologische Wissenschaften, 24, 3-20, 1996.

Bachmann, G. H., Müller, M., and Weggen, K.: Evolution of the Molasse Basin (Germany, Switzerland), Tectonophysics, 137, 77-92, 10.1016/0040-1951(87)90315-5, 1987.

Bachmann, G. H., Koch, K., Müller, M., and Weggen, K.: Ergebnisse und Erfahrungen bei der Exploration in den Bayerischen Alpen, Erdoel-Erdgas-Zeitschrift, 97, 127-133, 1981.

Budach, I., Moeck, I., Lüschen, E., and Wolfgramm, M.: Temporal evolution of fault systems in the Upper Jurassic of the Central German Molasse Basin: case study Unterhaching, International Journal of Earth Sciences, 107, 635-653, 10.1007/s00531-017-1518-1, 2018.

Couzens-Schultz, B. A. and Azbel, K.: Predicting pore pressure in active fold-thrust systems: An empirical model for the deepwater Sabah foldbelt, Journal of Structural Geology, 69, 465-480, 10.1016/j.jsg.2014.07.013, 2014.

Drews, M. C. and Duschl, F.: Overpressure, vertical stress, compaction and horizontal loading along the North Alpine Thrust Front, SE Germany, Marine and Petroleum Geology, 143, 10.1016/j.marpetgeo.2022.105806, 2022.

Drews, M. C., Bauer, W., Caracciolo, L., and Stollhofen, H.: Disequilibrium compaction overpressure in shales of the Bavarian Foreland Molasse Basin: Results and geographical distribution from velocity-based analyses, Marine and Petroleum Geology, 92, 37-50, 2018.

Drews, M. C., Hofstettter, P., Zosseder, K., Shipilin, V., and Stollhofen, H.: Predictability and mechanisms of overpressure in the Bavarian Foreland Molasse Basin: An integrated analysis of the Geretsried GEN-1 Deep Geothermal Well, Geoth. Energy, 8:20, 10.1186/s40517-019-0121-z, 2020.

Drews, M. C., Seithel, R., Savvatis, A., Kohl, T., and Stollhofen, H.: A normal-faulting stress regime in the Bavarian Foreland Molasse Basin? New evidence from detailed analysis of leak-off and formation integrity tests in the greater Munich area, SE-Germany, Tectonophysics, 755, 1-9, 10.1016/j.tecto.2019.02.011, 2019.

Drews, M. C., Shatyrbayeva, I., Bohnsack, D., Duschl, F., Obermeier, P., Loewer, M., Flechtner, F., and Keim, M.: The role of pore pressure and its prediction in deep geothermal energy drilling – examples from the North Alpine Foreland Basin, SE Germany, Petroleum Geoscience, 28, 10.1144/petgeo2021-060, 2022.

Flechtner, F. and Aubele, K.: A brief stock take of the deep geothermal projects in Bavaria, Germany (2018), PROCEEDINGS, 44th Workshop on Geothermal Reservoir Engineering, Stanford University, Stanford, California, February 11-13, 20192019.

Gardner, G. H. F., Gardner, L. W., and Gregory, A. R.: Formation velocity and density - the diagnostic basics for stratigraphic traps, Geophysics, 39, 770-780, 1974.

Großmann, J., Hofmann, N., Pamer, R., Spörlein, T., Pechnig, R., Knapp, D., Clauser, K., Karp, T., and Günther, D.: Abgeschlossene Arbeiten zur Digitalisierung geophysikalischer Grundlagendaten in Bayern, Geologica Bavarica, 127, 115 p., 2024.

Kuhlemann, J. and Kempf, O.: Post-Eocene evolution of the North Alpine Foreland Basin and its response to Alpine tectonics, Sedimentary Geology, 152, 45-78, 10.1016/S0037-0738(01)00285-8, 2002.

Lemcke, K.: Zur nachpermischen Geschichte des nördlichen Alpenvorlands, Geologica Bavarica, 69, 5-48, 1973.

Lemcke, K.: Übertiefe Grundwässer im süddeutschen Alpenvorland, Bulletin der Vereinigung Schweiz. Petroleum-Geologen und -Ingenieure, 42, 9-18, 1976.

Lemcke, K.: Dreissig Jahre Oel- und Gassuche im süddeutschen Alpenvorland, Jahresberichte und Mitteilungen des Oberrheinischen Geologischen Vereins, 61, 305-317, 1979.

Leu, W., Mégel, T., and Schärli, U.: Geothermische Eigenschaften der Schweizer Molasse Tiefenbereich 0–500 m)—Datenbank für Wärmeleitfähigkeit, spezifische Wärmekapazität, Gesteinsdichte und Porosität, Bericht Schweizer Bundesamt für Energie, 2006.

Lohr, J.: Die seismischen Geschwindigkeiten der jüngeren Molasse im ostschweizerischen und deutschen Alpenvorland, Geophysical Prospecting, 17, 111-125, 10.1111/j.1365-2478.1969.tb02075.x, 1969.

Lohr, J.: Alpine stress documented by anomalous seismic velocities in the Molasse trough, Inter-Union Com. On Geodynamics, Sc. Rep., 38, 69-71, 1978.

515 Megies, T. and Wassermann, J.: Microseismicity observed at a non-pressure-stimulated geothermal power plant, Geothermics, 52, 36-49, 10.1016/j.geothermics.2014.01.002, 2014.

Müller, M. and Nieberding, F.: Principles of abnormal pressures related to tectonic developments and their implication for drilling activities (Bavarian Alps, Germany), in: Oil and Gas in Alpidic Thrusbelts and Basins of Central and Eastern Europe, edited by: Wessely, G., and Liebl., W., EAGE Spec. Pub., 119-126, 1996.

Müller, M., Nieberding, F., and Wanninger, A.: Tectonic style and pressure distribution at the northern margin of
520 the Alps between Lake Constance and the River Inn, Geol. Rundsch., 77, 787-796, 1988.

Ortner, H., Aichholzer, S., Zerlauth, M., Pilser, R., and Fügenschuh, B.: Geometry, amount, and sequence of thrusting in the Subalpine Molasse of western Austria and southern Germany, European Alps, Tectonics, 34, 1-30, 10.1002/2014TC003550, 2015.

Pfiffner, O. A.: Evolution of the north Alpine foreland basin in the Central Alps, Foreland Basins, 219-228, 1986.

525 Raiga-Clemenceau, J., Martin, J. P., and Nicoletis, S.: The concept of acoustic formation factor for more accurate porosity determination from sonic transit time data, SPWLA 27th Annual Logging Symposium 1986,

Reinecker, J., Tingay, M., Müller, B., and Heidbach, O.: Present-day stress orientation in the Molasse Basin, Tectonophysics, 482, 129-138, 10.1016/j.tecto.2009.07.021, 2010.

Rizzi, P. W.: Hochdruckzonenfrüherkennung in Mitteleuropa, Erdoel-Erdgas-Zeitschrift, 89, 249-256, 1973.

530 Schulz, I., Steiner, U., and Schubert, A.: Factors for the Success of Deep Geothermal Projects – Experience from the Bavarian Molasse Basin, Erdöl Erdgas Kohle, 133, 73-79, 2017.

Sclater, G. and Christie, P. A. F.: Continental stretching: An explanation of the Post-Mid-Cretaceous subsidence of the central North Sea Basin, Journal of Geophysical Research, 85, 3711-3739, https://doi.org/10.1029/JB085iB07p03711, 1980.

535 Seithel, R., Steiner, U., Müller, B., Hecht, C., and Kohl, T.: Local stress anomaly in the Bavarian Molasse Basin, Geoth. Energy, 3, https://doi.org/10.1186/s40517-014-0023-z, 2015.

Shatyrbayeva, I., Duschl, F., and Drews, M.: Drilling data-calibrated shale compaction models for pore pressure evaluation from geophysical well logs in the North Alpine Foreland Basin, SE Germany Petroleum Geoscience, doi.org/10.1144/petgeo2024-014, 2024.

540 Shatyrbayeva, I, Bohnsack, D., Duschl, F., and Drews, M. C.: Comparison and integration of pore pressure measurements and indicators from drilling data in a deep geothermal energy play in SE Germany, Geoenergy, 1, geoenergy2023-2038, 10.1144/geoenergy2023-038, 2023.

von Hartmann, H., Tanner, D. C., and Schumacher, S.: Initiation and development of normal faults within the German alpine foreland basin: The inconspicuous role of basement structures, Tectonics, 35, 1560-1574,
545 10.1002/2016TC004176, 2016.

Wyllie, M. R. J., Gregory, A. R., and Gardner, L. W.: Elastic wave velocities in heterogeneous and porous media, Geophysics, 21, 41-70, 1956.

Yang, Y. and Aplin, A. C.: Definition and practical application of mudstone porosity-effective stress relationships, Petroleum Geoscience, 10, 153-162, 10.1144/1354-079302-567, 2004.

550 Ziegler, M. O. and Heidbach, O.: The 3D stress state from geomechanical–numerical modelling and its uncertainties: a case study in the Bavarian Molasse Basin, Geothermal Energy, 8, 10.1186/s40517-020-00162-z, 2020.

Ziegler, M. O., Heidbach, O., Reinecker, J., Przybycin, A. M., and Scheck-Wenderoth, M.: A multi-stage 3-D stress field modelling approach exemplified in the Bavarian Molasse Basin, Solid Earth, 7, 1365-1382,
555 10.5194/se-7-1365-2016, 2016.

Zoback, M. D.: Reservoir Geomechanics, Reservoir Geomechanics, Cambridge University Press, 1-452 pp., 10.1017/CBO9780511586477, 2007.

Zweigel, J.: Eustatic versus tectonic control on foreland basin fill: Sequence stratigraphy, subsidence analysis, stratigraphic modelling, and reservoir modelling applied to the German Molasse basin, Contributions to
560 Sedimentary Geology, 20, X-140, 1998.